Spin waves and spin-state transitions in a ruthenate high-temperature antiferromagnet

H. Suzuki[1*], H. Gretarsson[1,2], H. Ishikawa[1,3], K. Ueda[1], Z. Yang[1], H. Liu[1], H. Kim[1,4,5], D. Kukusta[1], A. Yaresko[1], M. Minola[1], J. A. Sears[2], S. Francoual[2], H.-C. Wille[2], J. Nuss[1], H. Takagi[1,3,6], B. J. Kim[1,4,5], G. Khaliullin[1], H. Yavaş[2‡] and B. Keimer[1*]

[1]*Max-Planck-Institut für Festkörperforschung, Heisenbergstraße 1, D-70569 Stuttgart, Germany*

[2]*Deutsches Elektronen-Synchrotron DESY, Notkestraße 85, D-22607 Hamburg, Germany*

[3]*Institut für Funktionelle Materie und Quantentechnologien, Universität Stuttgart, 70569 Stuttgart, Germany*

[4]*Department of Physics, Pohang University of Science and Technology, Pohang 790-784, South Korea*

[5]*Center for Artificial Low Dimensional Electronic Systems, Institute for Basic Science (IBS), 77 Cheongam-Ro, Pohang 790-784, South Korea and*

[6]*Department of Physics, University of Tokyo, Bunkyo-ku, Tokyo 113-0033, Japan*

(Dated: June 11, 2019)

‡ Current address: SLAC National Accelerator Laboratory, 2575 Sand Hill Rd, Menlo Park, CA 94025, USA

Ruthenium compounds serve as a platform for fundamental concepts such as spin-triplet superconductivity [1], Kitaev spin-liquids [2–5], and solid-state analogues of the Higgs mode in particle physics [6, 7]. However, basic questions about the electronic structure of ruthenates remain unanswered, because several key parameters (including Hund's coupling, spin-orbit coupling, and exchange interactions) are comparable in magnitude, and their interplay is poorly understood - partly due to difficulties in synthesizing large single crystals for spectroscopic experiments. Here we introduce a resonant inelastic x-ray scattering (RIXS) [8, 9] technique capable of probing collective modes in microcrystals of $4d$-electron materials. We observe spin waves and spin-state transitions in the honeycomb antiferromagnet $SrRu_2O_6$ [10] and use the extracted exchange interactions and measured magnon gap to explain its high Néel temperature [11–16]. We expect that the RIXS method presented here will enable momentum-resolved spectroscopy of a large class of $4d$ transition-metal compounds.

Inelastic neutron scattering (INS) experiments on magnetic collective modes yield highly specific information on the energy scale and spatial range of the electronic correlations that drive magnetic order, spin-liquid behavior, and unconventional superconductivity in quantum materials. However, since cm^3-sized single crystals required for INS are difficult to grow for ruthenates and other $4d$ transition metal compounds, our current understanding of electronic exchange and correlation effects in these materials is quite limited. Recent advances in x-ray instrumentation have enabled RIXS experiments on dispersive magnetic excitations in $3d$ and $5d$ metal compounds with energy resolution approaching the one of INS, and sensitivity sufficient to probe microcrystals and thin-film structures [17, 18]. In these experiments, the incoming photons are tuned to the dipole-active L-absorption edges of the metal atoms in the soft (hard) x-ray regimes for $3d$ ($5d$) metals, and the energy distribution of the scattered x-rays is measured by high-resolution analyzers. Analogous experiments on $4d$ metal compounds have thus far not been possible, because their L-edges are in a photon energy range between the soft and hard x-ray regimes (1-5 keV) that is difficult to access, and because suitable analyzers were not available.

We have built an intermediate-energy RIXS (IRIXS) spectrometer with an analyzer designed for measurements at the L-absorption edges of $4d$ metal compounds. Using this instrument, we obtained momentum-resolved spectra of spin waves and spin-state transitions from a microcrystal of $SrRu_2O_6$, a compound based on ruthenium-oxide honeycomb layers [10] whose high Néel temperature (T_N) of 563 K [11, 12] has recently inspired considerable theoretical work [13–16]. Models proposed to explain this observation include extended molecular orbitals on the hexagons

of the honeycomb lattice [13], and a dichotomy of localized and itinerant valence electrons residing in different Ru orbitals [16]. We show that the spin-wave dispersions extracted from the IRIXS data are well described by a Heisenberg model with nearest-neighbor exchange interactions, suggesting instead that the valence electrons are in the localized regime. At higher excitation energies, we detect spin-state transitions that allow us to determine the Hund's coupling of the $4d$ valence electrons. These results establish IRIXS as an incisive probe of the low-energy electronic structure of a large variety of ruthenates and other $4d$ metal compounds.

Figure 1a illustrates the crystal structure of $SrRu_2O_6$, which belongs to the hexagonal space group $P\bar{3}1m$ with lattice constants a = 5.200(2) Å and c = 5.225(2) Å. The ruthenium ions are octahedrally coordinated by oxygen ions and form a two-dimensional honeycomb network. $SrRu_2O_6$ is insulating and exhibits G-type antiferromagnetism below T_N [11, 12]. The Ru spins are oriented along the c-axis (Fig. 1b). We have carried out complementary resonant x-ray diffraction measurements to confirm the long-range magnetic order in our samples (see Supplementary Information).

While the nominal Ru valence of 5+ in the octahedral crystal field dictates three electrons in the $4d$ t_{2g} orbitals, a neutron powder diffraction study revealed a local magnetic moment of 1.4 μ_B per Ru atom [12], which is significantly lower than 3 μ_B expected for the high-spin $S = 3/2$ configuration. We synthesized hexagonal single crystals with typical diameter of $\sim$ 50 μm (Fig. 1c) using a hydrothermal technique (see Methods), which cannot be scaled up to yield crystals with dimensions required for INS. Alternative spectroscopic tools are therefore required to map out the magnetic collective modes and test the diverse models that have been proposed to explain the high Néel temperature and the moment reduction in $SrRu_2O_6$ [13–16]. This situation (which is also encountered in numerous other ruthenium compounds) has motivated the development of the IRIXS spectrometer.

Figure 1d,e shows a schematic of the IRIXS spectrometer and the scattering geometry. The incident x-rays were monochromatized by a pair of asymmetric Si(111) crystals and focused onto the sample (see Methods for details). They are linearly π-polarized and the scattering angle 2θ is fixed at 90°. This geometry significantly suppresses the elastic charge (Thomson) scattering, allowing us to detect low-energy magnetic excitations. Since the Ru_2O_6 honeycomb layers are sandwiched by the chemically inactive Sr layers (Fig. 1b), the inter-plane magnetic interaction can be treated as weak, as we will see below. Hereafter, the momentum transfer is expressed in terms of the in-plane component ($\boldsymbol{q}$), which was scanned by rotating the sample angle θ_i. The measurement paths in the $\boldsymbol{q}$ space are shown in Fig. 1f. The azimuthal angle ϕ is fixed at 0° for

the measurement along the (-H, 0) direction, and at -30° for the (-H, -H) direction.

Figure 2a,b shows raw (uncorrected) Ru L_3 RIXS spectra of $SrRu_2O_6$ along the (-H, 0) and (-H, -H) directions, respectively. In contrast to soft x-ray RIXS, the large incident photon momentum of IRIXS allowed us to map out the dispersion relations of the electronic excitations over the entire first Brillouin zone. The spectra exhibit three distinct features. First, low-energy sinusoidally dispersive peaks (red circles in Fig. 2a,b) emanate from the antiferromagnetic ordering vector $\boldsymbol{q} =$ (-1, 0) and have maxima at $\boldsymbol{q} =$ (-0.5, 0) along the (-H, 0) direction and at (-0.33, -0.33) along the (-H, -H) direction. Second, there are additional pronounced peaks at $\sim$ 0.65 eV (green triangles in Fig. 2a,b), which do not show any dispersion within the experimental error. Finally, one also observes a broad continuum with an onset of $\sim$ 0.4 eV. To visualize the momentum dependence of the scattering intensity, we show a color map of the RIXS data in Fig. 2c. The intensity of the low-energy branch is maximal at the antiferromagnetic ordering vector and vanishes at $\boldsymbol{q} = 0$, as expected for spin waves (magnons). Based on the dispersion relation and the intensity distribution, the dispersive low-energy excitations can therefore be assigned to single magnons. As discussed below, we assign the nondispersive feature at higher energies to intra-ionic spin-state transitions between $S = 3/2$ and $S = 1/2$ configurations, and the continuum to electron-hole excitations across the Mott gap. Fig. 2d schematically summarizes the decomposition of the full IRIXS spectra.

Having demonstrated the capability of IRIXS to detect single-magnon excitations, we now analyze the low-energy IRIXS spectra and discuss their implications for the magnetic interactions. Figure 3a,b shows the decomposition of the spectra into an elastic background (dotted black line) and the magnon peak (red line), based on least-squares fits to two Lorentzian profiles convoluted with the experimental resolution. The agreement of the experimental data and the total intensity resulting from the fits (green lines) allows us to accurately determine the dispersion and spectral weight of the magnon feature as a function of $\boldsymbol{q}$ (Fig. 3c,d). One notices a magnon gap of 36 meV at $\boldsymbol{q} = (-1, 0)$, reflecting the c-axis spin anisotropy. The magnon branch disperses up to 183 meV, both at $\boldsymbol{q} =$ (-0.5,-0.5) and (-0.33,-0.33).

To determine the exchange interactions between Ru spins from the experimental magnon dispersion, we use the following minimal spin Hamiltonian:

$$\mathscr{H} = J \sum_{<ij>} \boldsymbol{S}_i \cdot \boldsymbol{S}_j - K \sum_i S_{iz}^2, \tag{1}$$

where $\boldsymbol{S}_i = (S_{ix}, S_{iy}, S_{iz})$ is the spin $S = 3/2$ operator at site i, J is an isotropic Heisenberg interaction between nearest-neighbor Ru spins, and K is a uniaxial single-ion anisotropy term which

orients the spins along the c-axis ($K > 0$). The inter-plane coupling is assumed to be weak and is neglected. We apply the linear spin-wave approximation to the Hamiltonian to obtain the theoretical magnon dispersion (see Supplementary Information). There are two fitting parameters, JS and K/J, and the best fit is obtained with $JS = 65$ meV and $K/J = 0.028$ (dotted line in Fig. 3c). The agreement between the fit results and the IRIXS data demonstrates that the two-dimensional nearest-neighbor Heisenberg interaction and the small anisotropy term of $KS = 1.8$ meV are sufficient to describe the magnetic excitations. The slight discrepancy between experimental and theoretical curves along the (-H, -H) direction can be improved by introducing a second-nearest-neighbor coupling J_2, but it is clear that J_2 is much smaller than J. Monte-Carlo simulations (see Supplementary Information) using the experimental JS and K/J values reproduce the high $T_N \sim 500$ K. The large spin-orbit-induced magnon gap of 36 meV (420 K) suppresses low-energy fluctuations and thus plays a key role in stabilizing magnetic long-range order. These JS and K/J values are reproduced by density-functional LDA+$U_{\rm eff}$ (local density approximation plus Coulomb repulsion) calculations with moderate $U_{\rm eff} = 1.5$ eV (see Supplementary Information), supporting the model used and the fitting procedure. The same calculations also reproduce the electron-hole continuum revealed in the IRIXS spectra at high energies.

Figure 3d shows a comparison between the experimental magnon intensity (defined as the total area of the magnon peak) and the intensity calculated from RIXS operators for t_{2g} orbital systems [19] (see Supplementary Information for details). The $\boldsymbol{q}$ dependence for small $|H|$ is well reproduced by the theory, and the deviations at larger $|H|$ can be attributed to experimental uncertainties arising from the comparable dimensions of the IRIXS beam spot and the single-crystal samples. For small θ_i angles (large $|H|$), the small crystal captures only a part of the incident photons, so that the scattering intensity is reduced.

Finally, we discuss the origin of the pronounced peaks at ~ 0.65 eV and the mechanism of moment reduction in $SrRu_2O_6$. In the t_{2g}^3 electronic configuration in the cubic crystal field, the intra-ionic Coulomb interaction (intra-orbital U and inter-orbital U') and the Hund's coupling J_H produce several multiplets. The ground state is given by the orbitally-nondegenerate state with high-spin $S = 3/2$. The low-spin ($S = 1/2$) multiplets ^2E_g and $^2T_{1g}$ are located at the excitation energy $\sim 3J_H$ (where the relation $U' = U - 2J_H$ is assumed), and the $^2T_{2g}$ multiplet at $\sim 5J_H$. We thus assign the 0.65 eV peaks to a spin-state transition to the ^2E_g and $^2T_{1g}$ multiplets (see Fig. 2d), based on the strong intensity and the absence of energy dispersion. We thus obtain an experimental value of $J_H \sim 0.25$ eV, which is significantly smaller than the Ru^{5+} ionic value.

This indicates strong hybridization between the Ru t_{2g} and O $2p$ orbitals, reducing the magnetic moment from the value expected for isolated $S = 3/2$ ions.

The transition to the high-energy $^2T_{2g}$ multiplet at $\sim 5J_H$ (> 1 eV) is not clearly resolved in the IRIXS data. In order to explain this observation, we consider the trigonal distortion Δ (see Supplementary Information). Positive Δ (trigonal compression) enhances the intensity of the $3J_H$ transitions, whereas it strongly reduces that of the $5J_H$ transitions, so that it is hidden in the electron-hole continuum. Importantly, positive $\Delta \sim 0.25$ eV naturally reproduces the single-ion anisotropy K [the second term in eq. (1)] that opens the magnon gap. Since the orbital angular momentum $L = 0$ in the $S = 3/2$ ground state, first-order perturbation by the spin-orbit coupling does not lift its fourfold degeneracy. However, second-order perturbations involving higher-energy multiplet levels split the ground state quartet into a lower-lying $S_z = \pm 3/2$ doublet and higher-energy $S_z = \pm 1/2$ states, stabilizing the c-axis spin orientation.

In conclusion, we have successfully observed dispersive magnons in $SrRu_2O_6$ with Ru L_3 RIXS. The magnon dispersion is well described by the spin-wave theory of the two-dimensional Heisenberg Hamiltonian with a small anisotropy term. The predominance of nearest-neighbor exchange interactions obviates the need to invoke extended molecular orbitals which are expected to generate longer-range interactions [13]. On top of the electron-hole continuum above the Mott gap, we observe well-defined non-dispersive spectral features at ~ 0.65 eV, which originate from local spin-state transitions between $S = 3/2$ to $S = 1/2$ configurations. From an analysis of these data we estimate $J_H \sim 0.25$ eV, which is significantly smaller than the Ru^{5+} ionic value. This indicates strong hybridization between the Ru t_{2g} and O $2p$ orbitals and explains the reduced ordered moment in $SrRu_2O_6$, in agreement with theoretical work [13–16]. More broadly, our direct observation of Hund's intra-ionic multiplets and the description of magnons based on a Hamiltonian with only nearest-neighbor exchange interactions imply that $SrRu_2O_6$ is in the local-moment regime. The strong exchange interactions and large magnon gap observed by IRIXS explain its high Néel temperature. We note that the magnon gap is a consequence of the intra-ionic spin-orbit coupling, which has escaped attention in prior studies but turns out to be the ultimate driver of the high Néel temperature. The results demonstrate the potential of the newly developed IRIXS methodology to deepen our understanding of magnetism in $4d$ transition metal compounds.

Acknowledgements

We thank I. I. Mazin and Y. L. Xie for stimulating discussions. The project was supported by the European Research Council under Advanced Grant No. 669550 (Com4Com). We acknowledge DESY (Hamburg, Germany), a member of the Helmholtz Association HGF, for the provision of experimental facilities. The experiments were carried out at the beamlines P01 and P09 of PETRA III at DESY. H.S. and K.U. acknowledge financial support from the JSPS Research Fellowship for Research Abroad. H.S. is partially supported by the Alexander von Humboldt Foundation.

Author contributions

H.S., H.G., K.U., Z.Y., M.M. and H.Y. performed the RIXS experiments. H.I., J.N. and H.T. grew $SrRu_2O_6$ single crystals and performed sample characterization. H.G., H.C.W. and H.Y. designed the beamline and IRIXS spectrometer. H.S., H.G. and K.U. performed the magnetic REXS experiment with the help of J.A.S. and S.F.. H.S. analyzed the experimental data. H.L., H.K., D.K., A.Y., B.J.K. and G.K. carried out the theoretical calculations and contributed to the interpretation of the experimental data. H.S. and B.K. wrote the manuscript with comments from all co-authors. B.K. initiated and supervised the project.

Competing interests

The authors declare no competing interests.

Data availability

The data sets generated during and/or analysed during the current study are available from the corresponding author on reasonable request.

---

[1] Maeno, Y., Kittaka, S., Nomura, T., Yonezawa, S. & Ishida, K. Evaluation of spin-triplet superconductivity in Sr_2RuO_4. *J. Phys. Soc. Jpn.* **81**, 011009 (2012).

[2] Jackeli, G. & Khaliullin, G. Mott insulators in the strong spin-orbit coupling limit: From Heisenberg to a quantum compass and Kitaev models. *Phys. Rev. Lett.* **102**, 017205 (2009).

[3] Chaloupka, J., Jackeli, G. & Khaliullin, G. Kitaev-Heisenberg model on a honeycomb lattice: Possible exotic phases in iridium oxides A_2IrO_3. *Phys. Rev. Lett.* **105**, 027204 (2010).

[4] Sandilands, L. J., Tian, Y., Plumb, K. W., Kim, Y.-J. & Burch, K. S. Scattering continuum and possible fractionalized excitations in α-$RuCl_3$. *Phys. Rev. Lett.* **114**, 147201 (2015).

[5] Banerjee, A. *et al*. Proximate Kitaev quantum spin liquid behaviour in a honeycomb magnet. *Nat. Mater.* **15**, 733-740 (2016).

[6] Jain, A. *et al*. Higgs mode and its decay in a two-dimensional antiferromagnet. *Nat. Phys.* **13**, 633-637 (2017).

[7] Souliou, S.-M. *et al*. Raman scattering from Higgs mode oscillations in the two-dimensional antiferromagnet Ca_2RuO_4. *Phys. Rev. Lett.* **119**, 067201 (2017).

[8] Kotani, A. & Shin, S. Resonant inelastic x-ray scattering spectra for electrons in solids. *Rev. Mod. Phys.* **73**, 203–246 (2001).

[9] Ament, L. J. P., van Veenendaal, M., Devereaux, T. P., Hill, J. P. & van den Brink, J. Resonant inelastic x-ray scattering studies of elementary excitations. *Rev. Mod. Phys.* **83**, 705–767 (2011).

[10] Hiley, C. I. *et al*. Ruthenium(V) oxides from low-temperature hydrothermal synthesis. *Angew. Chem. Int. Ed.* **53**, 4423–4427 (2014).

[11] Tian, W. *et al*. High antiferromagnetic transition temperature of the honeycomb compound $SrRu_2O_6$. *Phys. Rev. B* **92**, 100404 (2015).

[12] Hiley, C. I. *et al*. Antiferromagnetism at $T > 500$ K in the layered hexagonal ruthenate $SrRu_2O_6$. *Phys. Rev. B* **92**, 104413 (2015).

[13] Streltsov, S., Mazin, I. I. & Foyevtsova, K. Localized itinerant electrons and unique magnetic properties of $SrRu_2O_6$. *Phys. Rev. B* **92**, 134408 (2015).

[14] Singh, D. J. Electronic structure and the origin of the high ordering temperature in $SrRu_2O_6$. *Phys. Rev. B* **91**, 214420 (2015).

[15] Hariki, A., Hausoel, A., Sangiovanni, G. & Kuneš, J. DFT+DMFT study on soft moment magnetism and covalent bonding in $SrRu_2O_6$. *Phys. Rev. B* **96**, 155135 (2017).

[16] Okamoto, S., Ochi, M., Arita, R., Yan, J. & Trivedi, N. Localized-itinerant dichotomy and unconventional magnetism in $SrRu_2O_6$. *Sci. Rep.* **7**, 11742 (2017).

[17] Braicovich, L. *et al*. Dispersion of magnetic excitations in the cuprate La_2CuO_4 and $CaCuO_2$ compounds measured using resonant x-ray scattering. *Phys. Rev. Lett.* **102**, 167401 (2009).

[18] Kim, J. *et al*. Magnetic excitation spectra of Sr_2IrO_4 probed by resonant inelastic x-ray scattering:

Establishing links to cuprate superconductors. *Phys. Rev. Lett.* **108**, 177003 (2012).

[19] Kim, B. J. & Khaliullin, G. Resonant inelastic x-ray scattering operators for t_{2g} orbital systems. *Phys. Rev. B* **96**, 085108 (2017).

Methods

Single crystals of $SrRu_2O_6$ were grown by a hydrothermal method. $Sr(OH)_2{\cdot}8H_2O$ (99%, Alfa Aesar, 0.130 g), $KRuO_4$ (97%, Alfa Aesar, 0.200 g) and 10 ml of deionized water were sealed in a Teflon-lined stainless steel autoclave with inner volume of 23 ml (Parr Instrument Company). The autoclave was heated to 473 K for 48 h and then cooled naturally to room temperature. Before the IRIXS experiments, the single crystals were aligned using an in-house x-ray diffractometer. The photograph of a $SrRu_2O_6$ single crystal (Fig. 1c) was taken using a camera attached to a Jobin Yvon LabRam HR800 micro-Raman spectrometer.

The RIXS experiments were performed at the newly-built IRIXS instrument at Dynamics Beamline P01 at PETRA III at DESY, which delivers a high flux of intermediate-energy photons. The incident energy was tuned to the Ru L_3 absorption edge (2837.5 eV) and monochromatized using an asymmetrical Si(111) channel-cut $(+,-)$ monochromator (ΔE = 100 meV). The polarization of the incident beam was in the horizontal scattering plane (π polarization). The polarization of the scattered x-rays was not analyzed. The x-rays were focused to a beam spot of $20 \times 20\ \mu m^2$. Scattered photons from the sample were collected at $2\theta = 90^\circ$ (horizontal scattering geometry) using a SiO_2 $(10\bar{2})$ (ΔE = 60 meV) diced spherical analyzer with a 1 m arm, equipped with a rectangular (100 (H) $\times$ 36 (V) mm^2) mask and a charge-coupled device camera, both placed in the Rowland geometry. The exact position of the elastic (zero energy loss) line was determined by measuring non-resonant scattering spectra from silver paint deposited next to the samples. The overall energy resolution of the IRIXS spectrometer at the Ru L_3-edge was 140 meV, as determined from the full-width-half-maximum of the silver paint spectra. The measurements were performed at 10 K, well below T_N.

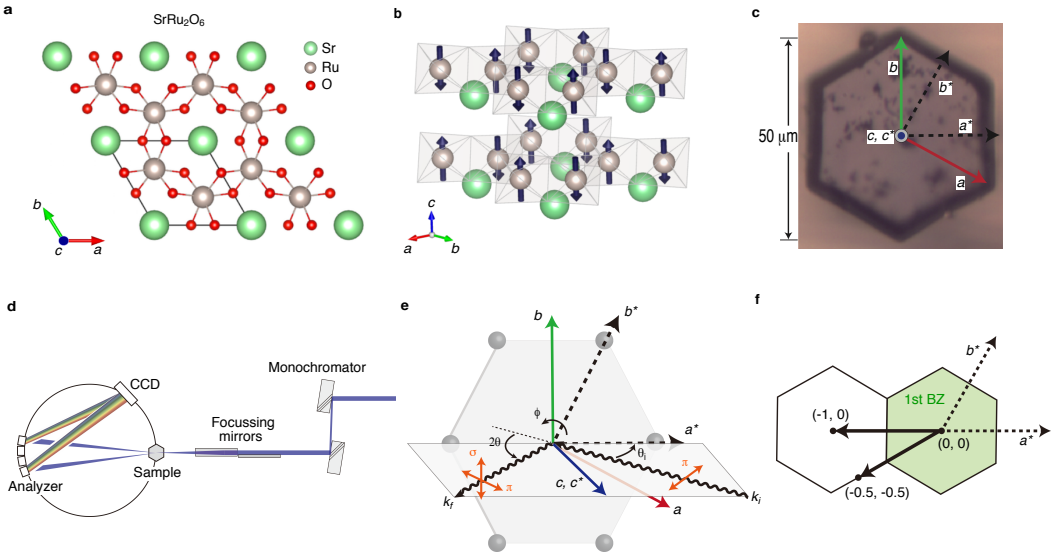

Figure 1 | Magnetic structure, intermediate-energy resonant inelastic x-ray scattering (IRIXS) spectrometer, and scattering geometry. **a**, Crystal structure and **b**, G-type antiferromagnetic order of $SrRu_2O_6$. Arrows *a*-*c* represent the crystallographic *a*-*c* axes. In **b**, RuO_6 clusters are shown by gray-shaded octahedra. The magnetic easy axis is along the *c*-axis. **c**, Photograph of a $SrRu_2O_6$ single crystal. The silver area is the top hexagonal surface parallel to the *ab*-plane and the black region is the edge of the crystal. Arrows a^*-c^* represent the reciprocal lattice vectors. **d**, Schematic of the IRIXS spectrometer. The incident x-ray photons are monochromatized by an asymmetrical Si(111) channel-cut and focussed to the sample. The energy of scattered x-rays is analyzed with a SiO_2 diced spherical analyzer (illustrated by rainbow) and collected with a charge-coupled device (CCD) camera. **e**, Scattering geometry for IRIXS experiments. The incoming x-rays with momentum $\boldsymbol{k}_i$ are linearly π-polarized and the polarization of the outgoing x-rays with momentum $\boldsymbol{k}_f$ is not analyzed. The scattering angle 2θ is fixed at 90° and the in-plane momentum transfer $\boldsymbol{q}$ is changed by rotating the sample angle θ_i. The azumuthal angle ϕ is used to change the measurement path. **f**, Measurement paths in the $\boldsymbol{q}$ space. The green-shaded area represents the first Brillouin zone (BZ).

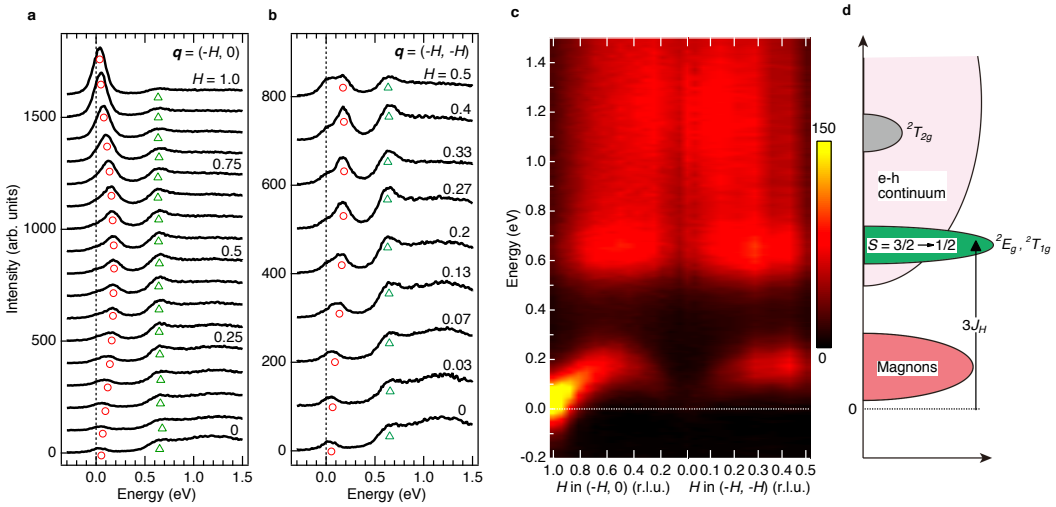

Figure 2 | IRIXS spectra of $SrRu_2O_6$. **a**, Raw Ru L_3 IRIXS spectra of $SrRu_2O_6$ along the (-H, 0) direction (in reciprocal lattice units) taken at 10 K, well below the Néel temperature. The in-plane momenta are equally spaced between $\boldsymbol{q}$ = (0, 0) and (-1, 0). The magnon peak positions determined by spectral fitting (Fig. 3) are denoted by red circles. The peak positions of the spin-state transitions, determined by finding the local maxima of smoothed spectra, are denoted by green triangles. **b**, IRIXS spectra along the (-H, -H) direction. **c**, Color map of the IRIXS intensity in panels **a** and **b**. Elastic peaks were subtracted for better visualization of the low-energy features. **d**, Schematic illustration of the elementary excitations. The low-energy excitations are the collective spin excitations (magnon) within the spin $S = 3/2$ sector. The intra-ionic multiplets ^2E_g and $^2T_{1g}$ with $S = 1/2$ are located at the excitation energy of $\sim 3J_H$ (J_H is the intra-ionic Hund's coupling). The higher multiplet $^2T_{2g}$ is hidden in the electron-hole (e-h) continuum.

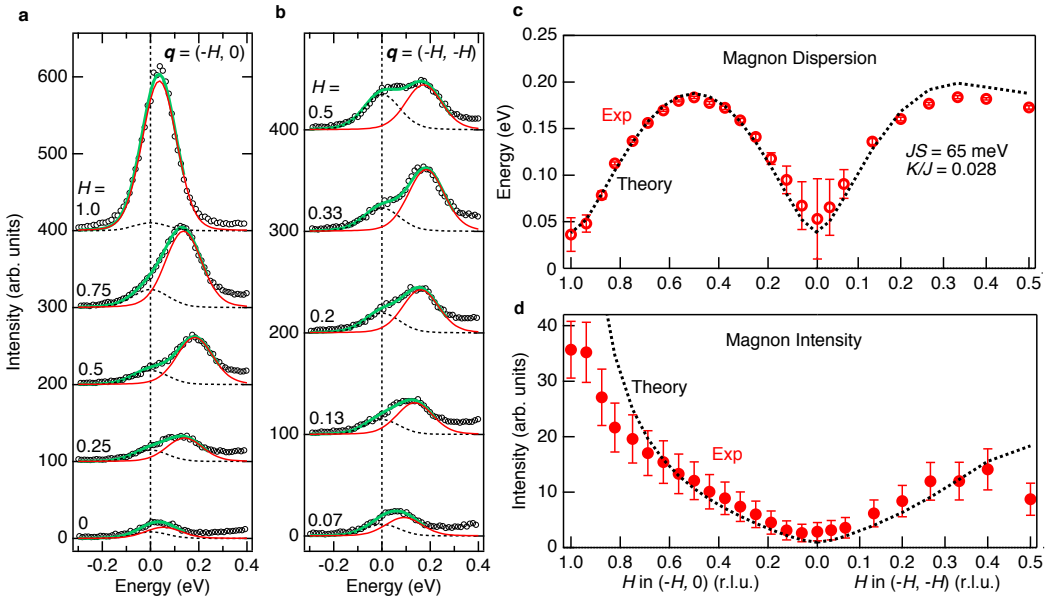

Figure 3 | **Magnon dispersion and intensity**. **a,b**, Decomposition of low-energy IRIXS spectra into the elastic background (dotted black line) and magnon peak (red line). The spectra were fitted to two Lorentzian functions convoluted with the experimental resolution of 140 meV. The total fitted spectra are shown as green lines. **c**, Magnon dispersion as a function of in-plane $\boldsymbol{q}$. The error bars represent the standard deviation of the fitting procedure. The dotted line shows the results of a fit of the magnon dispersion to the spin-wave theory defined in equation (1), where J is the Heisenberg exchange and K is the coefficient of the single-ion anisotropy term. **d**, Magnon intensity. The error bars indicate the statistical error. The dotted line indicates the RIXS intensity calculated from the spin-wave theory with the best-fit parameters.

Supplementary Information for
Spin waves and spin-state transitions in a ruthenate high-temperature antiferromagnet

H. Suzuki[1*], H. Gretarsson[1,2], H. Ishikawa[1,3], K. Ueda[1], Z. Yang[1], H. Liu[1],
H. Kim[1,4,5], D. Kukusta[1], A. Yaresko[1], M. Minola[1], J. A. Sears[2],
S. Francoual[2], H.-C. Wille[2], J. Nuss[1], H. Takagi[1,3,6], B. J. Kim[1,4,5],
G. Khaliullin[1], H. Yavaş[2] and B. Keimer[1*]

[1]*Max-Planck-Institut für Festkörperforschung, Heisenbergstraße 1, D-70569 Stuttgart, Germany*
[2]*Deutsches Elektronen-Synchrotron DESY, Notkestraße 85, D-22607 Hamburg, Germany*
[3]*Institut für Funktionelle Materie und Quantentechnologien, Universität Stuttgart, 70569 Stuttgart, Germany*
[4]*Department of Physics, Pohang University of Science and Technology, Pohang 790-784, South Korea*
[5]*Center for Artificial Low Dimensional Electronic Systems,*
Institute for Basic Science (IBS), 77 Cheongam-Ro, Pohang 790-784, South Korea and
[6]*Department of Physics, University of Tokyo, Bunkyo-ku, Tokyo 113-0033, Japan*

I. Static antiferromagnetic order of $SrRu_2O_6$

To confirm the static G-type antiferromagnetic (AFM) order in our $SrRu_2O_6$ single crystals, we performed resonant magnetic diffraction experiments at the Ru L_3 absorption edge at the beamline P09 of PETRA III at DESY. Figure S1a,b shows scans around the AFM Bragg peak at $\boldsymbol{q} = (1, 0, 1.5)$, along the $(H, 0, 0)$ and $(0, 0, L)$ directions. The measurement was done at 300 K, using the same photon energy (2837.5 eV) as that used for the RIXS experiments presented in the main text. The observation of the pronounced magnetic Bragg peak confirms the G-type AFM order. Moreover, the sharp profile with the full width half maximum of 7×10^{-4} r.l.u. both along the H and L directions demonstrates the long range magnetic order (correlation lengths > 1000 unit cells). Figure S1c shows the incident photon energy dependence of the peak intensity. The clear resonance profile around the Ru L_3 absorption edge further confirms its magnetic origin.

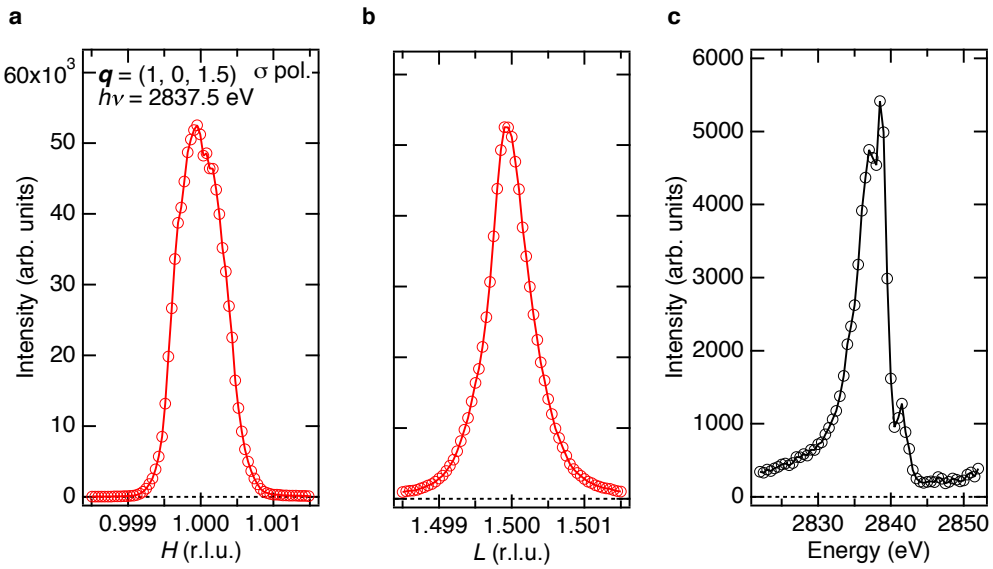

Figure S1 | Antiferromagnetic Bragg peak observed by resonant magnetic diffraction at the Ru L_3 edge. **a,b**, Scans around the antiferromagnetic Bragg peak at $\boldsymbol{q} = (1, 0, 1.5)$, along the $(H, 0, 0)$ and $(0, 0, L)$ directions, respectively. The measurement was done at 300 K, using photons with energy $h\nu = 2837.5$ eV. The incident photons are σ-polarized and the polarization of the scattered photons is not analyzed. **c**, Incident energy dependence of the peak intensity.

II. Magnon dispersion

To describe the magnons in $SrRu_2O_6$, we use the following nearest-neighbor Heisenberg exchange J Hamiltonian, supplemented by a single-ion anisotropy K term:

$$\mathscr{H} = J \sum_{<ij>} \boldsymbol{S}_i \cdot \boldsymbol{S}_j - K \sum_i S_{iz}^2. \tag{1}$$

The interlayer spin coupling is assumed to be weak (see Section V below) and is neglected at this point. Then, the results depend on the in-plane momentum $\boldsymbol{q} = (q_x, q_y)$ only. The Bragg point is at $(q_x, q_y) = \frac{4\pi}{3a}(1,0)$ or its equivalent positions.

Within the linear spin wave approximation, the magnon dispersion is obtained as follows (in units of JS):

$$\omega_q = 3\sqrt{\kappa^2 - |\gamma_q|^2} \ , \tag{2}$$

where $\gamma_q = \alpha_q + i\beta_q$, and

$$\begin{aligned} \kappa &= 1 + \frac{2}{3}\frac{K}{J} \ , \\ \alpha_q &= \frac{1}{3}\left[\cos(q_x a) + 2\cos(\tfrac{1}{2}q_x a)\cos(\tfrac{\sqrt{3}}{2}q_y a)\right], \\ \beta_q &= \frac{1}{3}\left[\sin(q_x a) - 2\sin(\tfrac{1}{2}q_x a)\cos(\tfrac{\sqrt{3}}{2}q_y a)\right]. \end{aligned} \tag{3}$$

Using the results of the previous work [1], the RIXS operator corresponding to the magnon sector can be written as $R_M = \frac{2}{3}(\boldsymbol{\varepsilon} \times \boldsymbol{\varepsilon}') \cdot \boldsymbol{S}$, where $\boldsymbol{\varepsilon}$ and $\boldsymbol{\varepsilon}'$ stand for the incoming and outgoing light polarizations. Calculating the dynamical spin susceptibility using the above Hamiltonian, we find the RIXS intensity $I_{q,\omega} = \frac{1}{\pi}\langle R_M R_M \rangle''_{q,\omega}$ as follows:

$$I_{q,\omega} = \frac{2}{9}\, S\, f(\theta)\, \frac{\kappa - \alpha_q}{\sqrt{\kappa^2 - \alpha_q^2 - \beta_q^2}}\, \delta(\omega - \omega_q) \ . \tag{4}$$

The function $f(\theta) = \frac{1}{2}(1 + \cos^2\theta)$, where θ is the angle between incoming light $\boldsymbol{k}_i$ and sample ab-plane, originates from averaging over directions of the outgoing polarization $\boldsymbol{\varepsilon}'$.

The function $f(\theta)$ can be expressed via the ratio $r = \frac{|\boldsymbol{q}|}{|\boldsymbol{Q}|}$ between the length of the in-plane momentum $|\boldsymbol{q}| = \sqrt{q_x^2 + q_y^2}$ and the total momentum transfer $|\boldsymbol{Q}|$:

$$f(\theta) = \frac{3}{4} + \frac{r\sqrt{1 - r^2}}{2} \ . \tag{5}$$

In the present experimental setup, we have $r = \frac{3a}{4\pi}\sqrt{q_x^2 + q_y^2}\,\cos\frac{\pi}{4}$.

Two different in-plane directions (-H, 0) and (-H, -H) are measured in the experiment. For comparison with the data, we express the above equations in terms of H.

A. (-H, 0) direction

For the (-H, 0) direction, the magnon dispersion is (in units of JS):

$$\omega_q = 2\sqrt{2} \cdot \sqrt{\frac{3}{2}\frac{K}{J}\left(1 + \frac{1}{3}\frac{K}{J}\right) + \sin^2(\pi H)} \ . \tag{6}$$

The intensity is $I_q\ \delta(\omega - \omega_q)$ with

$$I_q = \frac{4}{9}\, S\, f(\theta) \cdot \frac{1}{\omega_q} \cdot \left[\frac{K}{J} + \sin^2\left(\frac{2\pi}{3}H\right) + 2\sin^2\left(\frac{\pi}{3}H\right)\right] \ . \tag{7}$$

In terms of H, the parameter r in Eq. (5) reads as $r = \frac{1}{\sqrt{2}}\,|H|$.

B. (-H, -H) direction

For the (-H, -H) direction, the magnon dispersion is (in units of JS):

$$\omega_q = 3 \cdot \sqrt{\left(1 + \frac{2}{3}\frac{K}{J}\right)^2 - \left[1 - \frac{4}{3}\sin^2(\pi H)\right]^2} \ . \tag{8}$$

The intensity is $I_q\ \delta(\omega - \omega_q)$ with

$$I_q = \frac{2}{9}\, S\, f(\theta) \cdot \sqrt{\frac{\frac{K}{J} + 2\sin^2(\pi H)}{3 + \frac{K}{J} - 2\sin^2(\pi H)}} \ . \tag{9}$$

The parameter r in Eq. (5) in this case is $r = \sqrt{\frac{3}{2}}\,|H|$.

III. Density-functional-theory calculations of spin order parameter and constants J and K

Band structure calculations were performed for the experimental crystal structure using the relativistic linear muffin-tin orbital (LMTO) method as implemented in the PY LMTO computer code [2] and Perdew-Burke-Ernzerhof (PBE) parametrization of the generalized gradient approximation (GGA) to the exchange-correlation potential [3]. Matrix elements of the spin-orbit coupling (SOC) were added to the LMTO Hamiltonian at the variational step. The rotationally invariant implementation of the local density approximation plus Coulomb repulsion (LDA+U) method was used [4].

The strength of the isotropic exchange coupling J was estimated from scalar relativistic calculations. First, we performed self-consistent calculations for a collinear AFM configuration with Ru moments aligned along the c axis. Then, a single iteration was run for a number of non-collinear configurations in which the moment directions of the two Ru sublattices deviated by an angle θ from the c axis. The deviation from collinear AFM order was kept sufficiently small ($\theta \leq 20^\circ$) to ensure that the magnitude of the calculated Ru moment decreased by less then 4%. J was estimated by mapping the dependence of the band energy on the angle $\alpha = 180^\circ - 2\theta$ between the magnetizations of the two Ru sublattices onto an isotropic Heisenberg model. In the limit of small θ this approach becomes equivalent to using the magnetic force theorem [5]. Self-consistent LDA+U calculations with constrained Ru magnetization directions performed for selected values of $U_{\rm eff}$ show that the use of the magnetic force theorem for $SrRu_2O_6$ may give a value of J which differs from the total energy estimate by $\sim$10%.

The interlayer exchange coupling was estimated by comparing the total energy of the collinear AFM configuration to that of a spin spiral with a wave vector $\boldsymbol{q} = (0,0,\pi/c)$ which gives AFM order of the Ru moments along the c axis.

Finally, the anisotropy constant K was obtained from the difference of the total energies calculated taking into account the SOC for two collinear AFM configurations with the Ru magnetization parallel to the a and c crystallographic axes.

The experimentally observed spin order parameter is reduced from the density-functional-theory (DFT) result $S_{\rm DFT}$ by the zero-point spin contraction $\delta S_{\rm SW}$:

$$\langle S \rangle = S_{\rm DFT} - \delta S_{\rm SW}. \tag{10}$$

For an isotropic Heisenberg antiferromagnet on a 2D honeycomb lattice, the linear spin wave (SW) approximation gives $\delta S_{\rm SW} = 0.258$ [6], consistent with series expansion results for large spins $S > 1/2$ [7]. In the present case, the single ion anisotropy induced magnon gap should reduce the $\delta S_{\rm SW}$ value. We have calculated the linear SW reduction using the observed anisotropy parameter $K/J = 0.028$, and obtained $\delta S_{\rm SW} = 0.19$. The experimentally observed value $\langle S \rangle$ = 0.715 [8], so we aim to get $S_{\rm DFT} \simeq 0.9$. Using the DFT plus U method with different U values, we calculate the spin order parameter $\langle S \rangle$, the exchange constant J and the anisotropy K. While the results obtained within the GGA (the first column in Table I) show a significant deviation from the experimental values, the inclusion of a $U_{\rm eff}$ value of 1.5 eV (the second column) gives reasonable fits of all the three parameters. Note that the DFT result for the local spin of about 0.956 is less than $S = \frac{3}{2}$ for Ru^{5+}. This reduction can be attributed to a covalence effect, $\delta S_{\rm cov}$, which is about 0.54 and indicates rather strong pd-mixing in this compound.

IV. High-energy RIXS spectra: Intra-ionic multiplet transitions and electron-hole continuum

The intra-ionic Coulomb interaction and Hund's exchange J_H split the t_{2g}^3 electron configuration of the Ru^{5+} ion into several multiplets: an orbitally nondegenerate ground state accommodating a spin $S = 3/2$ quartet, low-spin $S = 1/2$ terms ^2E_g and

	GGA	$U_{\rm eff}$ = 1.5 eV	Experiment
$S_{\rm DFT}$	0.619	0.956	
$\langle S\rangle = S_{\rm DFT} - \delta S_{\rm SW}$	0.389	0.766	0.715 [8]
JS (meV)	60	74	65 (this work)
K/J	0.067	0.026	0.028 (this work)

TABLE I: Comparison of the spin order parameter and interaction constants obtained by density-functional-theory calculations and experiment. From the experimentally observed magnetic moment $1.43\mu_B$ at $T = 7.5$ K [8], we get $\langle S\rangle = 0.715$ (assuming $g \simeq 2$). The quantum spin wave reduction $\delta S_{\rm SW} = 0.19$ is calculated within the linear spin wave approximation, including the effect of the observed single ion anisotropy magnon gap.

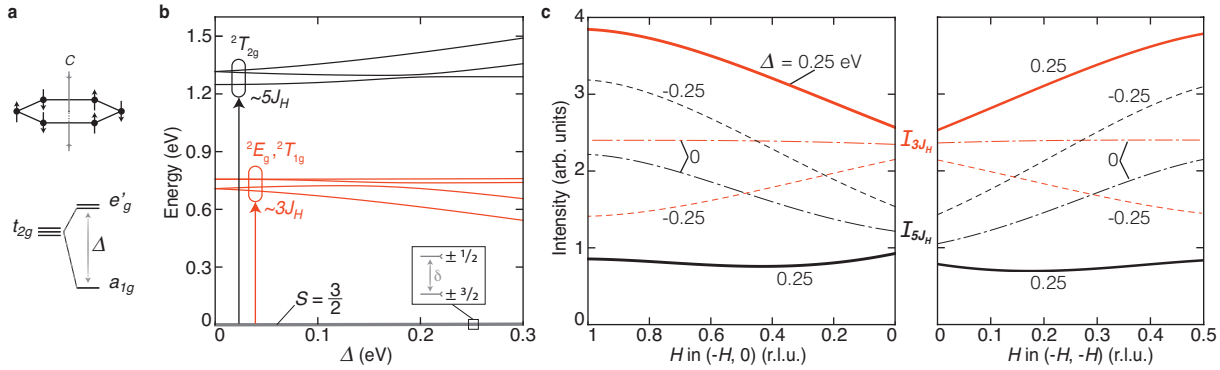

Figure S2 | Level structure and RIXS intensities. a. The trigonal compression along the c-axis splits the t_{2g} orbital level into a doublet e'_g and a singlet a_{1g} by Δ. **b**. The spin-orbital multiplet level structure of a t_{2g}^3 ion as a function of trigonal crystal field Δ. $J_H = 0.25$ eV and $\zeta = 0.15$ eV were used. Inset: the ground state $S = \frac{3}{2}$ level splits into two doublets, with $\pm 3/2$ states being lower for positive Δ (compressive distortion). **c**. The RIXS intensities I_{3J_H} (red lines) and I_{5J_H} (black lines) of $\sim 3J_H$ and $\sim 5J_H$ transitions, correspondingly, as a function of momentum transfer along (-H, 0) and (-H, -H). Different values of trigonal splitting are used: Δ = 0.25 eV (solid lines), Δ = 0 (dot-dashed lines), and Δ = -0.25 (dashed lines). At positive Δ = 0.25 eV, the intensities I_{3J_H} are much larger than I_{5J_H} for any momentum transfer H.

$^2T_{1g}$ with excitation energy $3J_H$, and a $^2T_{2g}$ multiplet at $5J_H$. Under a trigonal compression along the c-axis [see Fig. S2a] and spin-orbit coupling ζ, these multiplets further split forming the level structure shown in Fig. S2b. Note that the combined action of the trigonal field Δ and spin-orbit coupling also splits the $S = 3/2$ ground state by δ, which determines the sign and strength of the single ion anisotropy term $K = \delta/2$. The observed easy c-axis ($K > 0$) in $SrRu_2O_6$ implies then a positive Δ value. (Note that negative Δ as predicted by recent theory [9] would result in an easy-plane magnetism instead.) For $\Delta = 0.25$ eV, we find $\delta \simeq 2.5$ meV and $KS \simeq 1.9$ meV, consistent with the observed $KS \simeq 1.8$ meV.

Having the excited level wave-functions at hand, one can calculate the RIXS amplitudes of the intra-ionic $\sim 3J_H$ and $\sim 5J_H$ transitions. This is done numerically, within the so-called "fast-collision" approximation for RIXS operators [10]. The calculated intensities of these transitions are shown in Fig. S2c. It is noticed that the trigonal splitting Δ strongly influences the relative intensities of the $\sim 3J_H$ and $\sim 5J_H$ transitions. As Δ varies from negative to positive values (relevant to $SrRu_2O_6$), the intensity I_{3J_H} of the lower energy transitions $\sim 3J_H$ becomes dominant. Physically, the large spectral weight transfer between $\sim 3J_H$ and $\sim 5J_H$ transitions as a function of Δ originates from modifications of the wavefunctions of the orbitally degenerate excited levels by a trigonal crystal field.

In addition to intra-ionic multiplet transitions, electron-hole excitations across the Mott gap also contribute to the high-energy RIXS spectra. We have evaluated this contribution along the lines of previous work [11], using our *ab-initio* band structure for $SrRu_2O_6$. In the RIXS process, the electron propagates from the core level to the empty valence state with energy $E_{\boldsymbol{k}}$ and the core hole is annihilated by the electron from the level with energy $E_{\boldsymbol{k}+\boldsymbol{q}}$, so the final state is an excited electron-hole pair with energy $E_{\boldsymbol{k}} - E_{\boldsymbol{k}+\boldsymbol{q}}$ and momentum $\boldsymbol{q}$. The RIXS spectrum is a convolution of the densities of the occupied and empty valence

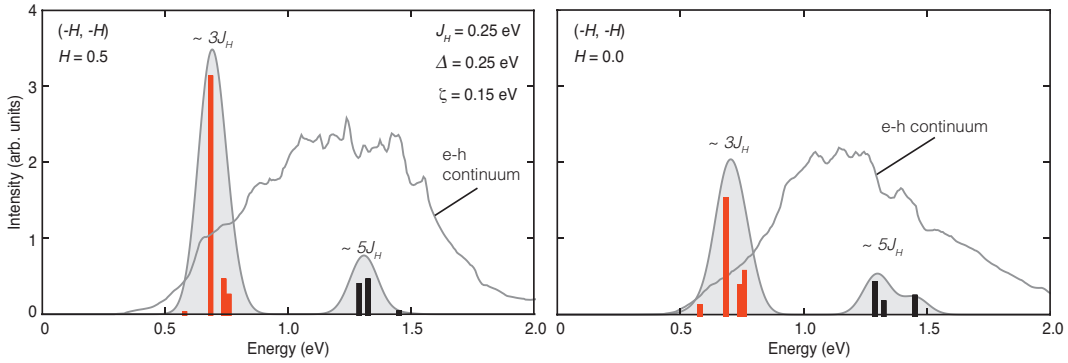

Figure S3 | Theoretical RIXS spectra. Calculated high-energy RIXS spectra at two representative momentum transfers. The vertical bars represent the intensities and energies of intraionic spin-orbital transitions, and are convoluted by Gaussians corresponding to the experimental resolution. We used $J_H = 0.25$ eV, $\Delta = 0.25$ eV, and $\zeta = 0.15$ eV. The intense peak at $\sim 3J_H$ is located near the lower edge of a broad electron-hole continuum, while the weak transitions near $\sim 5J_H$ fall well into the continuum.

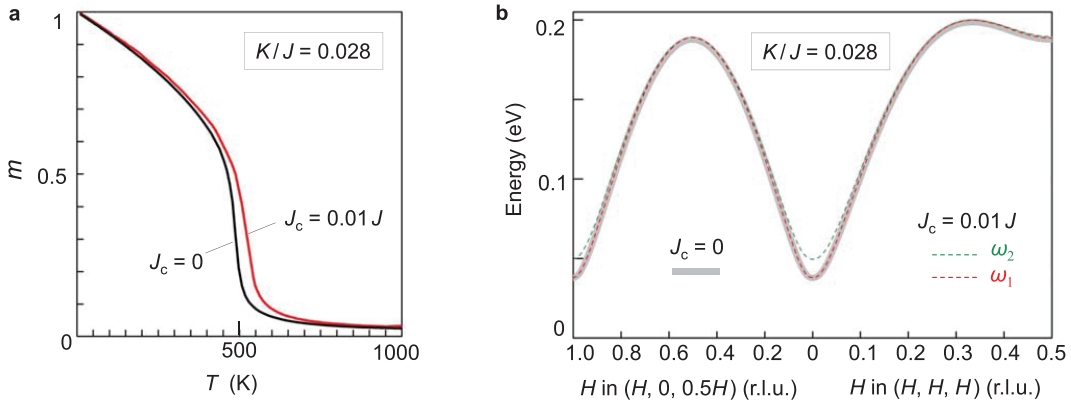

Figure S4 | Magnetic order parameter and magnon spectra. a. Classical Monte Carlo results for the staggered moment as a function of temperature, calculated at $J_c = 0$ (black line, system size 96×96) and $J_c = 0.01J$ (red line, system size 24×24×16). **b**. Magnon dispersion at $J_c = 0$ (thick grey line) and $J_c = 0.01J$ (dashed lines ω_1 and ω_2).

states, weighted by appropriate matrix elements.

The resulting electron-hole continuum is shown in Fig. S3, along with the intra-ionic multiplet transitions discussed above. The observed two-peak structure in the experiment - a relatively narrow peak ~ 0.65 eV followed by a broad continuum - is readily visible in our calculations, and can be associated with the intense $\sim 3J_H$ transition and the electron-hole continuum, correspondingly. We expect that the interaction between the local modes and the continuum (not considered here) will renormalize the $3J_H$ peak (downward shift and Fano-type broadening). The higher energy $\sim 5J_H$ transitions, which are strongly suppressed by the trigonal crystal field and fall into the electron-hole continuum, are unlikely to be resolved in the data.

V. Magnetic ordering temperature and interlayer coupling

The large magnon bandwidth $W \sim 183$ meV (~ 2100 K) implies that local AFM order is present well above the Néel temperature $T_N \sim 563$ K. This is similar to the case of quasi-two-dimensional cuprates [12], and explains the absence of a Curie-like paramagnetic regime above T_N. Although the overall energy scale W in $SrRu_2O_6$ is smaller than that in the cuprates, the Néel temperature is higher because of the large magnon gap Δ_m of 36 meV (~ 420 K). The gap is caused by the uniaxial single-ion anisotropy K term (which is allowed for $S = 3/2$ here, but absent in $S = 1/2$ cuprates). The magnon gap suppresses long wavelength spin fluctuations and gives a lower bound for the Néel temperature, *i.e.* $T_N > \Delta_m$. For a more quantitative estimate, we have performed classical Monte-Carlo simulations on a honeycomb lattice. Using the measured values of K and J, we obtain $T_N \sim 500$ K (see Fig. S4a), close to the experimental value. Coupling between the layers should further enhance T_N. Performing the DFT plus $U_{\text{eff}} = 1.5$ eV calculations as described above, we have evaluated the interlayer coupling and obtain $J_c = 0.01J$.

Monte-Carlo simulations including this coupling do indeed bring the Néel temperature even closer to that of $SrRu_2O_6$, see Fig. S4a. Overall, our data suggests that while the interlayer coupling is essential for establishing long-range coherence between the honeycomb planes, its influence on the Néel temperature is only minor. The uniaxial magnon gap of 36 meV plays the dominant role in defeating the infrared divergences related to the Mermin-Wagner theorem.

We note that due to the non-Bravias lattice structure of $SrRu_2O_6$, the interlayer coupling J_c splits the magnon modes into two, the lower ω_1 and higher (less intense) ω_2 branches. Their dispersion relations are (in units of JS):

$$\omega_1 = 3\sqrt{(\kappa+\tau)^2 - (|\gamma_q| + |\tau_q|)^2} \ , \tag{11}$$

$$\omega_2 = 3\sqrt{(\kappa+\tau)^2 - (|\gamma_q| - |\tau_q|)^2} \ , \tag{12}$$

where $\tau = \frac{2J_c}{3J}$ and $\tau_q = \tau\cos(q_z c)$. As shown in Fig. S4b, the splitting of the modes is about 10 meV, *i.e.* well below the current experimental resolution.

[1] Kim, B. J. & Khaliullin, G. Resonant inelastic x-ray scattering operators for t_{2g} orbital systems. *Phys. Rev. B* **96**, 085108 (2017).

[2] Antonov, V., Harmon, B. & Yaresko, A. *Electronic structure and magneto-optical properties of solids*. (Kluwer Academic Publishers, Dordrecht, Boston, London, 2004).

[3] Perdew, J. P., Burke, K. & Ernzerhof, M. Generalized gradient approximation made simple. *Phys. Rev. Lett.* **77**, 3865–3868 (1996).

[4] Yaresko, A. N., Antonov, V. N. & Fulde, P. Localized U $5f$ electrons in UPd_3 from LDA+U calculations. *Phys. Rev. B* **67**, 155103 (2003).

[5] Liechtenstein, A., Katsnelson, M., Antropov, V. & Gubanov, V. Local spin density functional approach to the theory of exchange interactions in ferromagnetic metals and alloys. *J. Magn. Magn. Mater.* **67**, 65 – 74 (1987).

[6] Weihong, Z., Oitmaa, J. & Hamer, C. J. Second-order spin-wave results for the quantum XXZ and XY models with anisotropy. *Phys. Rev. B* **44**, 11869–11881 (1991).

[7] Oitmaa, J., Hamer, C. J. & Weihong, Z. Quantum magnets on the honeycomb and triangular lattices at $T = 0$. *Phys. Rev. B* **45**, 9834–9841 (1992).

[8] Hiley, C. I. *et al*. Antiferromagnetism at $T > 500$ K in the layered hexagonal ruthenate $SrRu_2O_6$. *Phys. Rev. B* **92**, 104413 (2015).

[9] Okamoto, S., Ochi, M., Arita, R., Yan, J. & Trivedi, N. Localized-itinerant dichotomy and unconventional magnetism in $SrRu_2O_6$. *Sci. Rep.* **7**, 11742 (2017).

[10] Ament, L. J. P., van Veenendaal, M., Devereaux, T. P., Hill, J. P. & van den Brink, J. Resonant inelastic x-ray scattering studies of elementary excitations. *Rev. Mod. Phys.* **83**, 705–767 (2011).

[11] Arola, E., Strange, P. & Gyorffy, B. L. Relativistic theory of magnetic scattering of x rays: Application to ferromagnetic iron. *Phys. Rev. B* **55**, 472–484 (1997).

[12] Keimer, B. *et al*. Néel transition and sublattice magnetization of pure and doped La_2CuO_4. *Phys. Rev. B* **45**, 7430–7435 (1992).